Journal of Materials Chemistry B

Accepted Manuscript

This is an *Accepted Manuscript*, which has been through the Royal Society of Chemistry peer review process and has been accepted for publication.

Accepted Manuscripts are published online shortly after acceptance, before technical editing, formatting and proof reading. Using this free service, authors can make their results available to the community, in citable form, before we publish the edited article. We will replace this *Accepted Manuscript* with the edited and formatted *Advance Article* as soon as it is available.

You can find more information about *Accepted Manuscripts* in the Information for Authors.

Please note that technical editing may introduce minor changes to the text and/or graphics, which may alter content. The journal's standard Terms & Conditions and the Ethical guidelines still apply. In no event shall the Royal Society of Chemistry be held responsible for any errors or omissions in this *Accepted Manuscript* or any consequences arising from the use of any information it contains.

ROYAL SOCIETY OF CHEMISTRY

www.rsc.org/materialsB

Journal Name

ARTICLE

Nd^{3+}-doped $LiYF_4$ nanocrystals for the bio-imaging in the second near-infrared window

Received 00th January 20xx,
Accepted 00th January 20xx

DOI: 10.1039/x0xx00000x

www.rsc.org/

Xinyi Jiang,[a] Cong Cao,[a] Wei Feng*[a] and Fuyou Li*[a]

The fluorescent probes working in near-infrared (NIR) window have unparalleled advantages of high penetration depth and low interference from autofluorescence. In this paper we introduced a rare-earth doped nanoprobe working in this region with narrow emission band, high efficiency, and good bio-compatibility. The newly-developed host material $LiYF_4$ managed to strengthen the emission intensity and generate fine structure of the emission peaks. After optimization of the doping ratio of Nd^{3+} and surface modification, the $LiYF_4$: 5% Nd^{3+} probe could reach the penetration depth of 3–5 mm and could be successfully utilized in lymphatic imaging, with a signal-to-noise ratio of 14.8 *in vivo* and resolution of ~0.2 mm in circulatory imaging. This probe may be further used in bio-detection and the host material itself may replace the traditional $NaYF_4$ in some aspects of application.

Introduction

The development of luminescent probe, with its advantages of high sensitivity, high accuracy, fast feedback and absence of radiation, has opened a new area in bio-imaging.[1,2] In bio-imaging applications, light may be absorbed or scattered easily at shorter wavelengths like UV region and visible region, which harms the efficiency of these probes.[3] The autofluorescence from biological tissues also influences the final imaging result. Due to the aforementioned reasons, fluorescent probes working in the second near-infrared window (NIR II, 1,000–1,350 nm), where the interference from autofluorescence, absorption and scattering is minimal, are more propitious for intravital imaging,[4] especially ones with excitation and emission wavelength both inside the NIR II region.

However, the practical utilization of probes in NIR II window requires expensive detectors based on indium gallium arsenide (InGaAs) or mercury cadmium telluride (HgCdTe) sensors, which are expensive and still not widely used.[3] Meanwhile, the development of bio-compatible probes in NIR II window for imaging, like single-walled carbon nanotubes (SWNTs),[5-9] quantum dots (QDs)[10-15] and polymer fluorophores[16] remains in nascent stages. The SWNTs usually have a relatively broad emission band and low quantum yield which restrict their usage in imaging,[17,18] and the wide length distributions may affect their pharmacokinetic behavior, ultimately impeding its practical application.[19] For QDs, most of them are still affected by the potential problem of toxicity. The newly-developed silver chalcogenide QDs require upgrade in surface modification to ameliorate its quantum yield.[20] Therefore, it is meaningful to design a probe of narrower emission band, higher efficiency, controllable size and lower bio-toxicity.

Rare earth metals are commonly used for synthesizing nanomaterials for bioapplication. Their abundant 4f electrons allow researchers to tune the luminance in a wide range from UV to NIR using different doping ions. Meanwhile, the emission peaks generated from rare earth ions are sharp and resistant to impact from the outside environment. Apart from the outstanding luminescent properties, no serious bio-toxicity has been reported.[21] Recently, different kinds of rare-earth materials in NIR II range have also been developed, like rare-earth fluorides[22-24] and oxides for cancer targeting[25,26] and *in vivo* imaging.[27,28]

Herein, we introduce $LiYF_4$ to be the host material for our probe. As a member of rare earth fluorides, it possesses the merits of outstanding optical transparency and low phonon energy which can minimize the non-radiative energy loss.[29] Nd^{3+} was chosen to be the doping ion for its intrinsic NIR emissive luminescent properties. Numerous applications of Nd^{3+} ion in NIR region have been reported, from the widely-used Nd laser oscillators[30] to the newly-designed Nd^{3+}-sensitized solar batteries.[31] For bioapplication, the NIR emission of Nd has already been used in bio-imaging after subcutaneous injection[24, 32] or intravenous injection[33] on mouse model. It also showed great potential in intratumoral thermal detection[24] and photothermal treatment.[34] We combined it with $LiYF_4$ and designed the $LiYF_4$: Nd^{3+} nanoparticles (NPs) system which needs a few steps to be synthesized and has high luminescent efficiency. Laser at

[a] *Department of Chemistry & Institutes of Biomedical Science & State Key Laboratory of Molecular Engineering of Polymers, Fudan University, 220 Handan Road, Shanghai 200433, P. R. China*
** To whom correspondence should be addressed: fengweifd@fudan.edu.cn or fyli@fudan.edu.cn*

Electronic Supplementary Information (ESI) available: [details of any supplementary information available should be included here]. See DOI: 10.1039/x0xx00000x.

This journal is © The Royal Society of Chemistry 20xx

Please do not adjust margins

Journal of Materials Chemistry B Accepted Manuscript

808 nm, bringing less heat effect,[35,36] was applied to excite the Nd^{3+} ions and luminescent signals at 900 nm, 1,050 nm and 1,330 nm were designed as imaging signals. The as-prepared probe has relatively stronger emission compared to $NaYF_4$ NPs with the same doping ratio of luminescent ions, due to the special crystal structure of $LiYF_4$, [37, 38] and the desired superiorities of $LiYF_4$: Nd^{3+} have been proved in the bio-imaging applications.

Experimental

Materials

All the chemicals used were of analytical grade and were used without further purification. Deionized water was used throughout. Rare-earth oxides, RE_2O_3 (99.999%) (RE^{3+} = Y^{3+}, Nd^{3+}), NaOH, $LiOH·H_2O$, NH_4F, HCl, methanol, ethanol and cyclohexane were purchased from Sinopharm Chemical Reagent Beijing Co., Ltd.. Oleic acid, 1-octadecene and nitrosonium tetrafluoroborate ($NOBF_4$), were bought from Alfa Aesar Ltd.. Dimethyl sulfoxide (DMSO) was bought from Sigma-Aldrich Co. Ltd.. Ethylenediaminetetra(methylene phosphonicacid) (EDTMP) were gained from TCI (Shanghai) Development Co., Ltd.. All the doping ratios of RE^{3+} were calculated in molar in our experiments.

Synthesis of $LiYF_4$: x% Nd^{3+} (x = 1.0, 3.0, 5.0, 7.0, 10.0) NPs

The rare-earth chlorides used were synthesized by adding HCl into rare-earth oxides, followed by evaporating the remaining liquid to get solid powder. The NPs of $LiYF_4$ were synthesized using a specially-modified co-precipitation method. [39] A mixture of 1-x% mmol YCl_3, x% mmol $NdCl_3$, oleic acid (OA, 6 mL), 1-octadecene (15 mL) was added into a 100 mL three-necked flask at room temperature. The oxygen was moved out by vacuuming under vigorous magnetic stirring. Then, the system was heated to 130 °C to form clear and transparent solution. After the solution was cooled to 70 °C naturally, 8 mL of methanol solution containing $LiOH·H_2O$ (0.106 g) and NH_4F (0.148 g) were slowly added into the flask, and precipitates appeared in the solution. The mixture was stirred for 30 min and gradually got transparent again, guaranteeing the complete consumption of fluorides, and then it was heated to evaporate the methanol for 15 min, followed by vacuuming for 15 min to ensure the removal of methanol and water. After that, heat the solution to 300 °C under the protection of nitrogen atmosphere. The solution was held at the final temperature for 90 min after which it was allowed to cool to the room temperature prior to precipitation with absolute ethanol. The mixture was separated by centrifugation and the precipitates were collected and further purified by cyclohexane/ethanol (v/v 1:2) twice. The resulted NPs were dispersed in cyclohexane (10 mL) for further use.

Surface modification of $LiYF_4$: Nd^{3+} NPs

To make these NPs hydrophilic, add the as-prepared cyclohexane solution (5 mL) of NPs and cyclohexane (5 mL) into a centrifugal tube and then disperse them evenly under ultrasonic method. Add $NOBF_4$ into the solution until no more precipitate forms.[40] The precipitates were separated with centrifugation and re-dispersed in water (5 mL), and then we added ethanol drop by drop until the solution got transparent again. The NPs were separated with centrifugation and washed with water for several times. Then we dispersed them in water (5 mL). The bare NPs could be modified using different ligands. In our research we chose EDTMP as surface ligand for further biological applications. Add the water solution of bare NPs into EDTMP solution and separate the precipitates by centrifugation. Wash the excessive ligands away with water, and then re-disperse the EDTMP-modified NPs with water for further use.

Characterization

The morphologies of as-prepared $LiYF_4$: Nd^{3+} NPs were examined by a JEOL JEM-2010 low- and high-resolution (HR) transmission electron microscope operating at 200 kV. The samples were dispersed in cyclohexane and dropped onto a copper grid for TEM tests. The energy-dispersive x-ray analysis (EDXA) was also performed on this microscope. X-ray powder diffraction (XRD) measurements were performed at room temperature on a Bruker D4 diffractometer at a scanning rate of $1°·min^{-1}$ in the 2θ range of 10–80°, with graphite monochromated Cu Ka radiation (λ = 1.5406 nm). The NIR fluorescence spectrum was measured using Edinburgh Instruments FLS920 fluorescence spectrometer, equipped with an external 0–3 W adjustable laser (808 nm, Beijing Hi-Tech Optoelectronic Co., China) as the excitation source at room temperature. The collected range was from 830 nm to 1,400 nm. The quantum yield (QY) was measured at room temperature using Photo Technology International QM40 fluorescence spectrometer, equipped with a xenon lamp as the excitation source. The cyclohexane solution of $LiYF_4$: 5% Nd^{3+} NPs and pure cyclohexane (blank) were excited at 808 nm and the emission was collected from 750 nm to 1,150 nm. The numbers of absorption photons (N_{abs}) and emission photons (N_{em}) were recorded to calculate the QY using the following formula:

$QY\ (\%) = (N_{em} / N_{abs}) \times 100.$

Intragastric administration on a mouse model

All animal procedures were in agreement with the guidelines of the Institutional Animal Care and Use Committee. 0.2 mg (0.1 mL × 2 mg/mL) of EDTMP-$LiYF_4$: Nd^{3+} NPs were imbued to the stomachs of a nude mouse and a Kunming mouse, both purchased from the Second Military Medical University (Shanghai, China), by using gastric syringes. The NIR luminescence imaging was performed with the *in vivo* imaging system designed by our group.[41] We used 808 nm lasers as excitation source and Andor DU897 EMCCD as signal collector. The quantum efficiency of the CCD is shown in Fig. S6. The excitation intensity of 808 nm irradiation was kept below 400 mW/cm^2 and the exposure time was 1 s. Images of luminescent signals were analysed with Carestream MI SE. The

Journal of Materials Chemistry B Accepted Manuscript

This journal is © The Royal Society of Chemistry 20xx

Please do not adjust margins

signals were collected at wavelength > 980 nm. The transmittance of the 980 nm long-pass edge filter (Semrock BLP01-980R Optical Filter) is shown in Fig. S7.

Lymphatic mapping on a mouse model

1.0 mg (0.10 mL × 10 mg/mL) of EDTMP-$LiYF_4$: Nd^{3+} NPs were injected into nude mice from paw and footpad respectively. The NIR luminescence imaging was performed with the *in vivo* imaging system designed by our group as mentioned above. 24 h after injection we collected the imaging results *in vivo*, then the mouse were opened up at the site of lymph node and the lymph nodes were taken out for imaging afterwards. The excitation intensity of 808 nm irradiation was kept below 400 mW/cm^2 and the exposure time was 1 s. Images of luminescent signals were analysed with Carestream MI SE. The signals were collected at wavelength > 980 nm.

Blood vessel imaging on a mouse model

1.0 mg (0.20 mL × 5 mg/mL) of EDTMP-$LiYF_4$: Nd^{3+} NPs were injected into a nude mouse intravenously to test the resolution of blood vessel imaging. 2.0 mg (0.20 mL × 10 mg/mL) of EDTMP-$LiYF_4$: Nd^{3+} NPs were injected into a Kunming mouse intravenously to view the bio-distribution. The *in vivo* images were shot immediately. The NIR luminescence imaging was performed with the *in vivo* imaging system designed by our group as mentioned above. The excitation intensity of 808 nm irradiation was kept below 400 mW/cm^2 and the exposure time was 1 s. Images of luminescent signals were analysed with AndorSolis, Carestream MI SE and origin 8.0®. The signals were collected at wavelength > 980 nm.

Cytotoxicity assay

The *in vitro* cytotoxicity was measured using the methyl thiazolyltetrazolium (MTT) assay using HeLa cell line. Cells growing in log phase were seeded into a 96-well cell-culture plate (Corning Costar, Cambridge, MA, USA) and then incubated for 12 h at 37.5 °C under 5% CO_2,in RPMI-1640 (Invitrogen, Grand Island, NY, USA), supplemented with 10% heat-inactivated fetal bovine serum (FBS; Invitrogen), 50 IU/mL penicillin and 50 mg/mL streptomycin (Invitrogen). Solutions of 0–600 μg/mL EDTMP-$LiYF_4$: Nd^{3+} NPs were added to the well of the treatment group, and RPMI-1640 to the negative control group. The cells were incubated for 24 h at 37.5 °C under 5% CO_2. For a colorimetric MTT assay, DMSO was added to solubilize formazan and absorbance was measured at 562 nm. The following formula was used to calculate the viability of cell growth:

Cell viability (%) = (mean of Abs value of treatment group / mean of Abs value of control) × 100.

Histology of animal organs

Kunming mice were intravenously injected with 1.5 mg (0.15 mL × 10 mg/mL) of EDTMP-$LiYF_4$: Nd^{3+} NPs. Organs were harvested 1 day and 7 days after injection, fixed using paraformaldehyde, embedded in paraffin, sectioned and stained with hematoxylin and eosin (H&E). Organs from untreated animals were analysed as control.

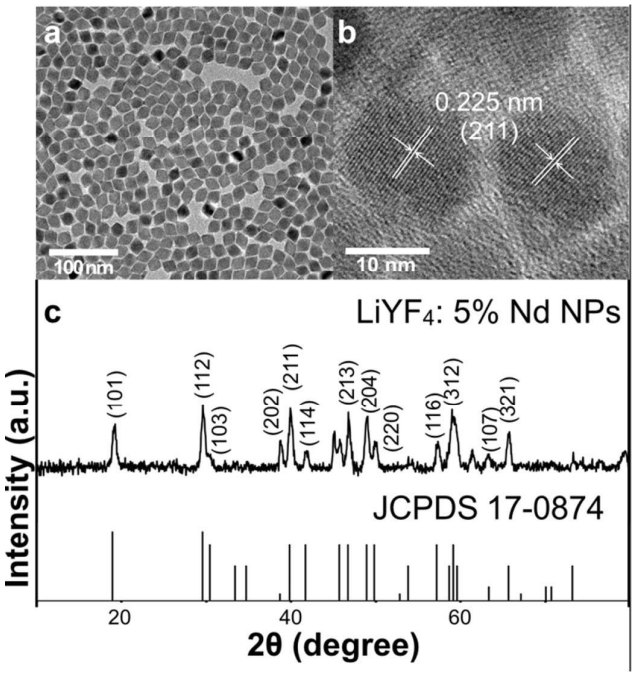

Fig. 1 (a) TEM image of $LiYF_4$: 5% Nd^{3+} NPs. Scale bar = 100 nm. (b) HR-TEM image of $LiYF_4$: 5% Nd^{3+}. Scale bar = 10 nm. (c) XRD pattern of $LiYF_4$: 5% Nd^{3+} NPs and the standard PDF card of tetragonal $LiYF_4$.

Result and discussion

Synthesis and characterization of $LiYF_4$: Nd^{3+} NPs

The synthesis of $LiYF_4$ nanocrystals in relatively large quantities has not been widely reported due to their special characteristics. Compared with the widely-used $NaYF_4$ nanocrystals, they also belong to rare earth fluorides, and possess similar rigid crystal lattice and ordered structure. The $LiYF_4$ structure is isomorphous with $CaWO_4$, with Li^+ at the spots of W^{4+} and Y^{3+} at the spots of Ca^{2+}.[37,42] The tetragonal $LiYF_4$ synthesized here showed an octahedral shape (Fig. 1a–b, Fig. S1a–e, g), which was also consistent with former researches.[29,38,43] The XRD patterns confirmed the special crystal structure and the high crystallinity of the nanocrystals. As shown in Fig. 1c and Fig. S1g, the planes could be smoothly fit to the standard PDF card (JCPDS 17-0784) of tetragonal $LiYF_4$. The peaks were broadened due to the small sizes of nanomaterials. The EDXA analysis proved the existance of Nd^{3+} (Fig. S2). With the increase in doping ratio of Nd^{3+}, the NPs grew larger from 18 to 30 nm at length and from 15 to 25 nm at width (Fig. S1a–e), with standard deviation of around 1–2 nm. And the phase of crystals did not show obvious change. The growing trend was possibly caused by the relatively larger radius of Nd^{3+} compared to that of Y^{3+}, which distorted the rigid arrangement of atoms in the lattice, since after implementing different reaction conditions this trend in size remained stubbornly.

Journal of Materials Chemistry B Accepted Manuscript

Please do not adjust margins

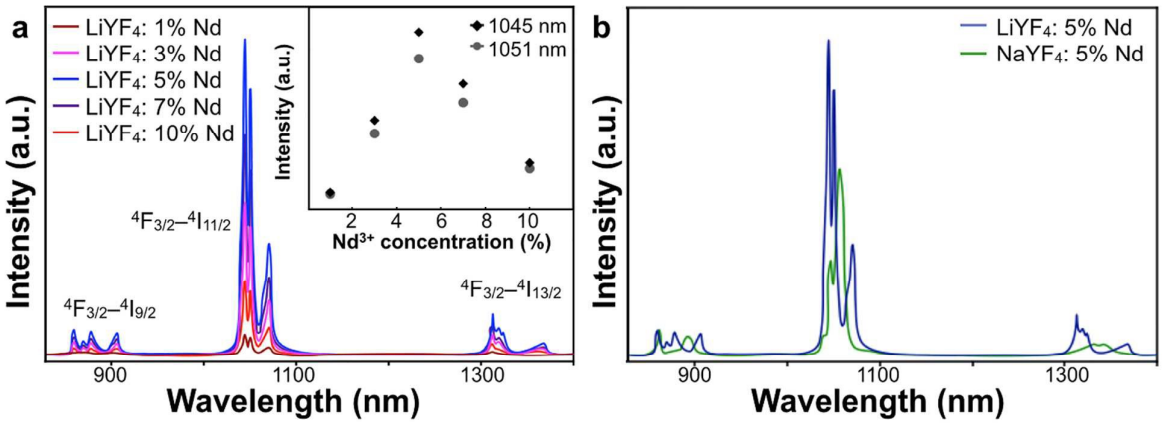

Fig. 2 (a) Fluorescence spectra of cyclohexane solution of OA-$LiYF_4$: x% Nd^{3+} NPs, x = 1.0, 3.0, 5.0, 7.0, 10.0. The inset shows the intensity of emissions at 1045 nm and 1051 nm as functions of Nd^{3+} ion concentration. (b) Fluorescence spectra of cyclohexane solution of OA-$LiYF_4$: 5% Nd^{3+} NPs and OA-$NaYF_4$: 5% Nd^{3+} NPs.

The luminescent properties of $LiYF_4$: Nd^{3+} NPs were characterized with fluorescent spectroscopy. Since the NPs were synthesized with the control of OA, they were ultimately covered with OA ligands on the surface. As a result, they were dispersible in organic solvents like cyclohexane, and the fluorescence spectra were measured in cyclohexane solution. As shown in Fig. 2, the emission was ascribed to the f–f electronic transitions of Nd^{3+}. The Nd^{3+} ions were excited from $^4I_{9/2}$ to $^4F_{5/2}$ by the laser of 808 nm, and then the transitions of $^4F_{3/2}$–$^4I_{9/2}$ (900 nm), $^4F_{3/2}$–$^4I_{11/2}$ (1,050 nm) and $^4F_{3/2}$–$^4I_{13/2}$ (1,330 nm) occurred and generated these emission peaks. The luminescent intensity increased when the doping ratio of Nd^{3+} was raised from 1% to 5%. However, after reaching the peaking emission intensity, it gradually fell at the doping ratios of 7% and 10%, which was possibly caused by the cross-relaxation among Nd^{3+} ions, between which the distance lowered as well. The QY of the $LiYF_4$: 5% Nd^{3+} NPs was tested in cyclohexane solution and reached 28% due to the simple process of luminance and relatively little energy loss from non-radiative transitions (Figure. S3).

We also synthesized Nd^{3+}-doped NPs based on the traditional host material, $NaYF_4$, as comparison. The size of $NaYF_4$ was controlled to be around 23 nm, which was comparable to the average size of $LiYF_4$ (Fig. S1f). The luminescent spectra of $NaYF_4$: Nd^{3+} NPs of different doping ratio, collected under the same test conditions, are shown in Fig. S4. Similarly, the

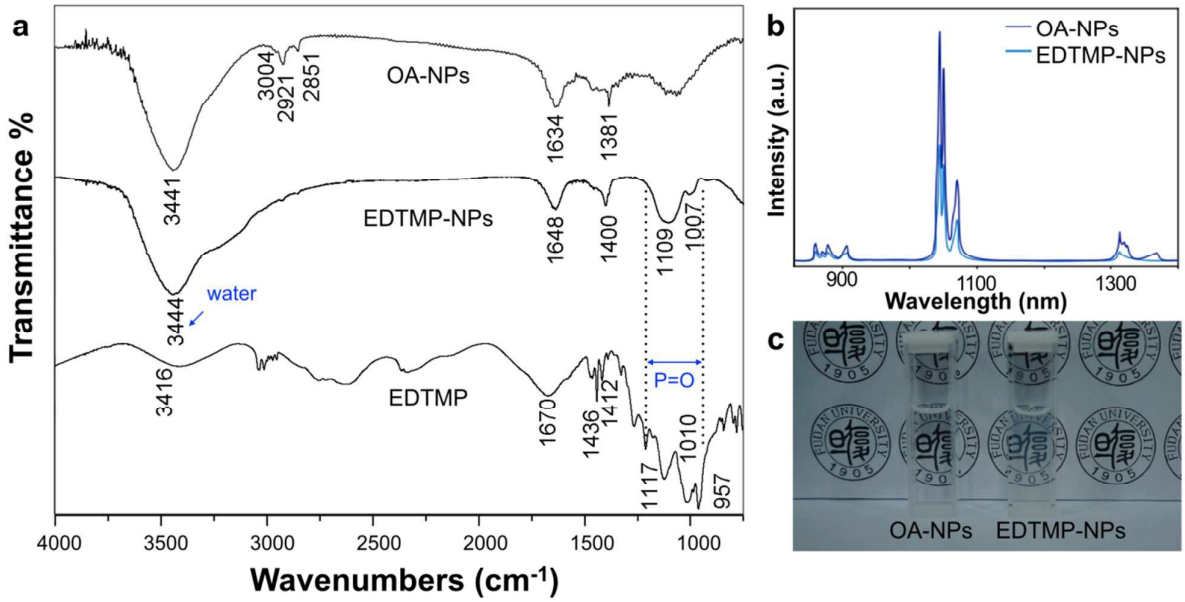

Fig. 3 (a) IR spectra of OA-$LiYF_4$: Nd^{3+} NPs, EDTMP-$LiYF_4$: Nd^{3+} NPs and pure EDTMP sample. (b) Fluorescence spectra of cyclohexane solution of OA-$LiYF_4$: 5% Nd^{3+} NPs and aqueous solution of EDTMP-$LiYF_4$: 5% Nd^{3+}. (c) Digital camera graph of cyclohexane solution of OA-$LiYF_4$: 5% Nd^{3+} NPs and aqueous solution of EDTMP-$LiYF_4$: 5% Nd^{3+} NPs.

This journal is © The Royal Society of Chemistry 20xx

Please do not adjust margins

Journal of Materials Chemistry B Accepted Manuscript

strongest intensity was achieved in $NaYF_4$: 5% Nd^{3+} NPs. However, $LiYF_4$: 5% Nd^{3+} NPs presented stronger emission intensity and the split of emission peaks was more delicate (Fig. 2b). Since the electric field of the surroundings produced a crystal field which exerted influence on the multiplets and caused the Stark splits, the tetragonal $LiYF_4$ crystal had relatively fewer symmetry properties, thus the energy levels of Nd^{3+} were changed by the crystal field, leading to stronger emission and more refined split.[36,37]

Then we chose to use the $LiYF_4$: 5% Nd^{3+} to conduct the following biological experiments. The surfaced ligands of NPs were washed using the reported method and then made hydrophilic with EDTMP.[40] The rare-earth nanoparticles capped with oleic acid will transform in the acidic physiological fluids, like lysosomes, resulting in pro-inflammatory effects and quenching of fluorescence. The coating of EDTMP could passivate the surfaces of the particles to lessen the transformation behaviour and lower the cytotoxicity, as well as preserve the fluorescence quality. Due to the strong coordination interaction between the central rare-earth atom and the ligand, it could be easily functionalized on the surface of bare $LiYF_4$: Nd^{3+} NPs.[21] The ligand exchange was successful as proven by the result of infrared (IR) spectroscopy (Fig. 3a). The OA-capped NPs showed the stretching vibration frequency at around 3,000 cm^{-1} of carbonic double bond and methene, and these peaks was noticeably reduced in the EDTMP-capped NPs. The EDTMP-capped NPs showed the specific absorption of P=O in EDTMP at 1,109 and 1,007 cm^{-1}, which was also substantiated by the strong absorbance around these wavelengths in the IR spectroscopy of pure EDTMP sample. The zeta-potential of EDTMP-capped NPs was -23.1 mV. These results confirmed the substitution of OA with EDTMP at the surface of the NPs. [21,44] The hydrophilic NPs were of perfect dispersibility and transparency as is shown in Fig. 3c. The hydrodynamic sizes of the water-phase NPs were also tested and no aggregation was observed (Fig. S5). After the ligand exchange process, the emission intensity decreased by about 50 percent while the position of the emission peaks did not change (Fig. 3b). It was possibly caused by the quenching of hydrophilic ligand and aqueous solution.

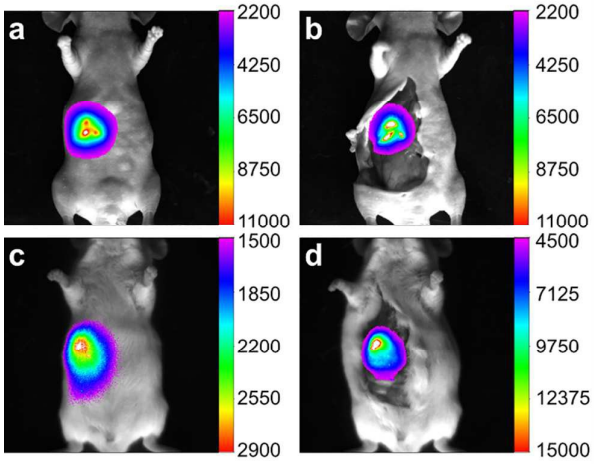

Fig. 4 NIR II images of EDTMP-$LiYF_4$: Nd^{3+} NPs after intragastric administration at the stomach of a (a) nude mouse, (b) nude mouse after removal of skin and fat tissues above, (c) Kunming mouse, (d) Kunming mouse after removal of skin and fat tissues above. The gain parameter of figure (c) and (d) is twice of that applied to figure (a) and (b).

Intragastric administration

To evaluate the penetration depth of imaging applications with EDTMP-$LiYF_4$: Nd^{3+} NPs, we conducted the experiment of intragastric administration on both nude mouse and Kunming mouse as shown in Fig. 4, using common Si-CCD as detector. The depth of mice's stomachs were around 3–5 mm for nude mice and 5–7 mm for Kunming mice, and we could still collect signals of high levels with the amount of injection of 0.2 mg (0.1 mL × 2 mg/mL). The skin of nude mouse was relatively thinner, so that the imaging quality did not improve a lot after removal of tissues above. For Kunming mouse covered by thick furs and skin, the fluorescence was low *in vivo*, so we had to raise the gain parameter of CCD detector to twice of that applied to the nude mouse. But it shall be noticed that with the inevitable impact caused by thick tissues, we were still able to collect signals strong enough for imaging and analysis. The fluorescence intensity increased significantly after opening up the mouse, by approximately an order of magnitude. The results showed the great penetration capacity of this NIR II probe and laid solid foundations for further imaging in lymphatic and vascular systems.

The luminance of mouse food in NIR II window has been reported.[22] Control experiments have also been performed under the same condition (Fig. S8). There did exist autofluorescence of the mice and mouse food, but the signals were very low (below 1500 counts) compared to the fluorescence of the materials (usually 2000 – c.a.60000 counts). There were several other imaging experiments based on the fluorescence of Nd in NIR II window after intravenous[32] or subcutaneous injection,[22,33] which have realized the imaging on mouse model on a basic level.

Lymphatic imaging

The lymphatic system is one of the common ways of tumor metastasis, so the imaging of lymphatic system is of great significance in the diagnosis and treatment of cancer. Herein, we injected the EDTMP-$LiYF_4$: Nd^{3+} NPs into the nude mice. In Fig. 5a–c, the NPs were injected through paw and axillary lymph node (pointed out with yellow arrows) was lightened. The emission intensity was already satisfying in *in vivo* imaging, which proved the outstanding detection depth, and we could almost see no autofluorescence, which was another advantage of NIR II imaging. The signal-to-noise ratio (SNR) reached 14.8 (Table S1). When the skin and fat tissue upon the lymph node were removed, it showed stronger emission exceeding the detection range of the CCD (shown as white color block, Fig. 5b), and better SNR no less than 18.9. After that we found the lymph node and took it out, to avoid damaging the CCD detector, we lowered the gain parameter by half and collected signals of almost the same intensity (Fig. 5c). The observation

Journal of Materials Chemistry B Accepted Manuscript

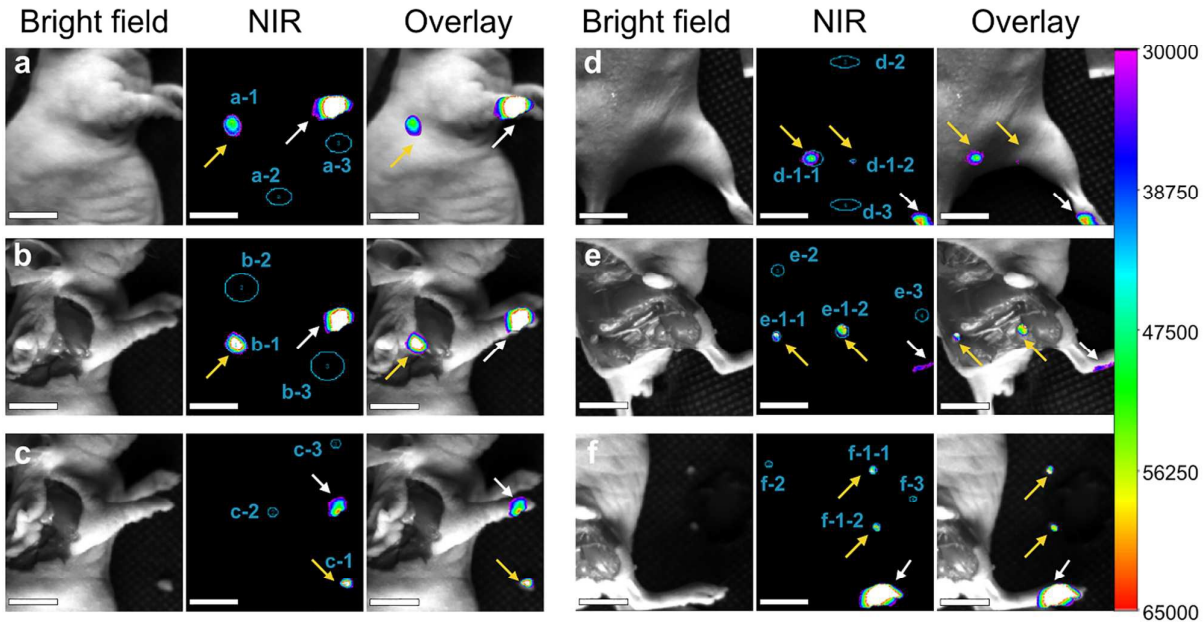

Fig. 5 NIR II imaging of lymph node 24 h after injection at the right paw of the nude mouse (a) *in vivo*, (b) after removal of skin and fat tissues above. (c) The removed axillary lymph node. NIR II imaging of lymph nodes 24 h after injection at the right footpad of the nude mouse (d) *in vivo*, (e) after removal of skin and fat tissues above the lymph nodes. (f) The removed lymph nodes around leg. Scale bar = 0.5 cm. All the lymph nodes are notified with yellow arrows and the inject site are marked with white arrows. The regions of interest (ROI) are marked using blue areas. The mean intensity of ROI 1(specific uptake), ROI 2 (nonspecific uptake) and ROI 3 (background) were collected for the signal-to-noise ratio (SNR) calculation (see Table S1).

result was further confirmed by histological analysis that lightened tissues were lymph nodes indeed (Fig. S11a). The injection at footpad was also carried out and two of the sentinel lymph nodes (pointed out with yellow arrows) were lightened (Fig. 5d–f), though the SNR was relatively lower (12.8, *in vivo*). The results were confirmed by histological analysis as well (Fig. S11b–c). Compared to other researches in NIR II lymphatic imaging,[2] our materials were distributed mainly in the lymphatic system and maintained a good imaging quality 24 h after injection, which was beneficial for potential usage in long-term tracing, meanwhile implying the extraordinary bio-stability and bio-compatibility.

Blood vessel imaging

Angiography is another important way of cancer diagnosis, since the development of tumor will inevitably involve the growth of new blood vessels.[45] In order to test the potential in practical application, we assessed the feasibility of EDTMP-$LiYF_4$: Nd^{3+} NPs in blood vessel imaging. Fig. 6 displays the imaging results of blood vessels of a nude mouse. At vascular bifurcations, fine vessels could be seen separately, demonstrating intuitively the high resolution of this probe. It was further verified by the intensity profiles along the red-dashed lines, in which different peaks of the signals of blood vessels could be easily identified in Fig. 6a, c, d, and fit to Gaussian functions (marked with red-dashed curves) to extract the width. Due to the inevitable absorbance and scattering of the tissues, we used the full width at half maximum (FWHM) to represent the widths of the vessels. Almost all the calculated widths were consistent with the expected values around 0.1–2.0 mm,[46] except one of them shown in Fig. 6d, reaching the width of 2.80 mm. This result was still reasonable, as this blood vessel could be seen much wider than all the other ones around it with the naked eye in the bright-field picture of it (Fig. 6e). These results proved that our probe could show the width of vessels veritably, from ~0.2 mm to ~3.0 mm, with little interference from biological tissues, reaching a commensurate resolution limit of Micro-CT.[46] Furthermore, in Fig. 6a, c, d, all the Gaussian fit was restricted to the artificially selected data range. To put it another way, the signal peaks could not be identified by common data processing softwares like origin® in a relatively large range. That might be caused by the narrow width of the peak composed of only a few data points (4–5), which were not enough for the software to identify the peaks automatically, and this problem could not be solved now because of the limited resolution of the CCD detector. Only limited pixels could be collected on a line of fixed length. So we tried to find the vessels wide enough to contain more data points to prove the ability of this probe to distinguish separate blood vessels. The ones in Fig. 6f were both the extension of *arteriacarotis*, and the signal peaks could be identified automatically from the background. The fitting result was also satisfying and the FWHM could also be directly read from the diagrams. It should be pointed out that though the apparent resolution was not as high as those of the reported SWNTs[46] and Ag_2S QDs,[2] the CCD detector used in our imaging experiment was Si-CCD, and the quantum efficiency was about 40 percent lower than that of

Journal of Materials Chemistry B Accepted Manuscript

This journal is © The Royal Society of Chemistry 20xx

Please do not adjust margins

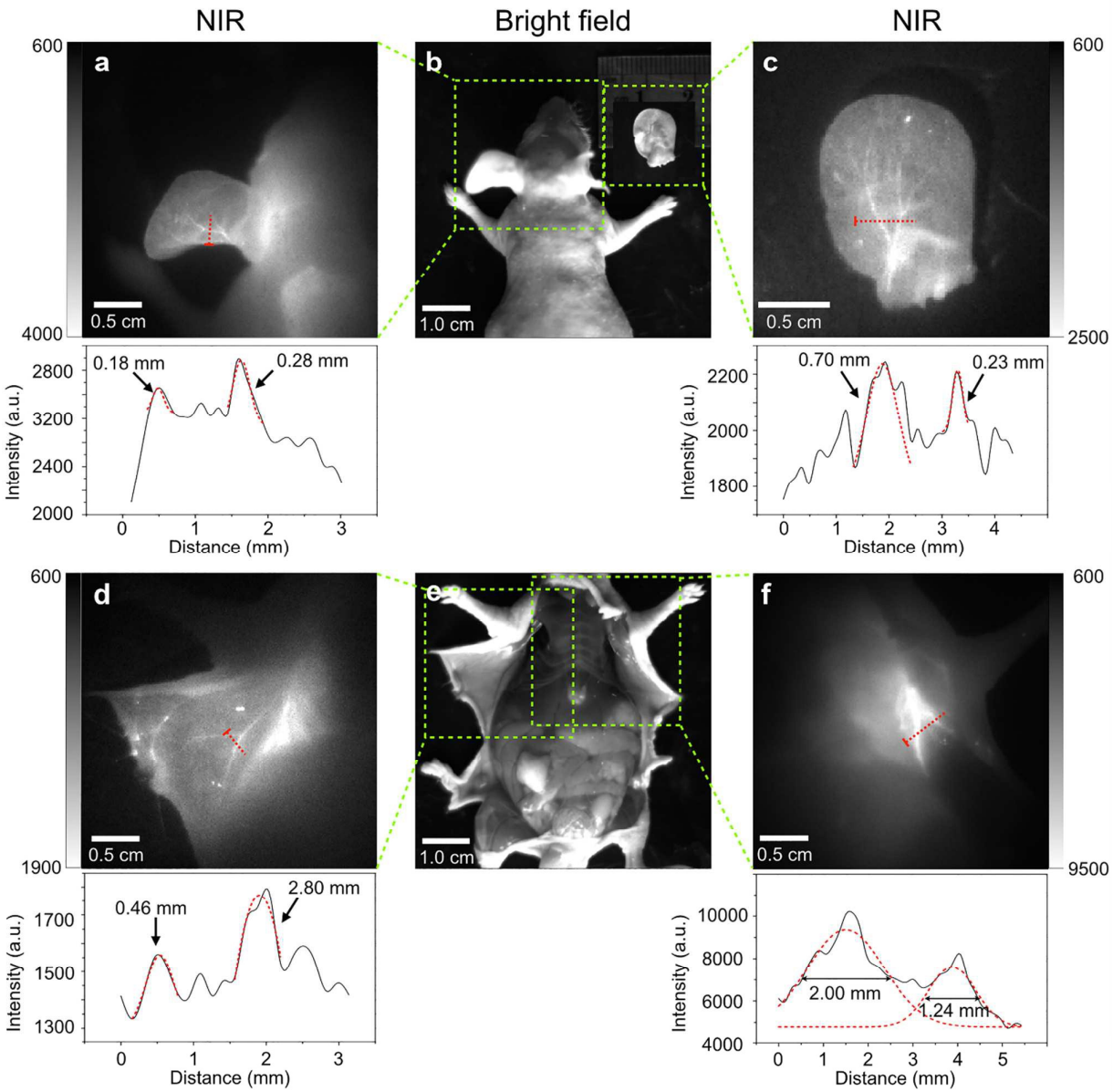

Fig. 6 (a) *In vivo* blood-vessel NIR II imaging of a nude mouse at left ear immediately after intravenous injection. (b) The bight-field picture of the nude mouse *in vivo*. The corresponding regions of NIR imaging are marked with green squares. (c) The NIR II imaging of the right ear cut immediately after intravenous injection. (d,f) *In situ* blood-vessel NIR II imaging of a nude mouse. (e) The bight-field picture of the nude mouse *in situ*. The corresponding regions of NIR imaging are marked with green squares. Cross-sectional fluorescence intensity profiles along red-dashed lines of the mouse are displayed at the bottom. The origin points (distance = 0) are presented with red short bars. Gaussian fits to the profiles are shown in red-dashed curves. The full width at half maximum is also marked in the diagrams.

InGaAs-CCD at the working wavelength.[3] The image was still clear enough to see the fine blood vessels of nude mice. Considering the high price of an InGaAs-CCD, this probe can be easily promoted for ordinary animal imaging requiring lower cost. The imaging quality might be improved by changing the activator ions and imaging system in further research.

Bio-distribution after intravenous injection

The distribution of this probe after intravenous injection was also tested. As shown in Fig. S9, the nanocrystals mainly aggregated in the liver of the mouse, showing a strong signal (SNR = 12.8, *in vivo*). It involved the elimination process of the nanomaterials from blood. It was corresponding to the result of histology test (Fig. S10) that the NPs did not accumulate in lung, so that the possibility of its causing damage in lung was low, while the risk of lung injury was often high when it comes to other nanomaterials.[47,48]

Test of bio-toxicity

One of the most important characteristics of an *in vivo* imaging probe is bio-compatibility. The possible bio-toxicity of EDTMP-$LiYF_4$: Nd^{3+} was assessed using MTT assay in HeLa cell line (Fig.

Journal of Materials Chemistry B Accepted Manuscript

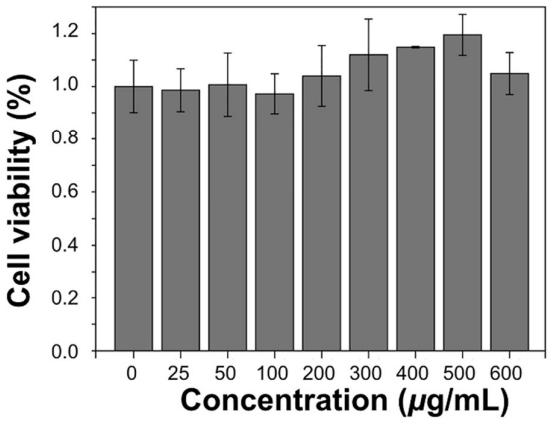

Fig. 7 Cytotoxicity of EDTMP-$LiYF_4$: Nd^{3+} NPs determined for Hela cells after 24 h of incubation.

7). The cell viability did not decrease with the increasing concentration of EDTMP-$LiYF_4$: Nd^{3+} NPs. Instead, it showed a growing trend as if the NPs exerted positive influence on the cells. The result is explicable since rare-earth fluorides can promote the growth of living things at low concentration.[49] So we may at least conclude that the NPs did not have apparent cytotoxicity. The histology test was also conducted and the H&E stained tissue section did not show obvious lesions in heart, liver, spleen, lung and kidney tissues as well (Fig. S10), which proved the good bio-compatibility of EDTMP-$LiYF_4$: Nd^{3+} NPs.

Conclusions

In brief, we successfully designed a simple and efficient NIR II probe for lymphatic and circulatory imaging. The newly-adopted host material, $LiYF_4$, enhanced the intensity and split of emission peaks and was of great bio-compatibility. The activator ion, Nd^{3+}, enabled excitation at 808 nm which gave out emission in NIR II window, enjoying the merits of high penetration depth and low autofluorescence. The quantum yield of the nanoparticles in cyclohexane was determined to be 28%. This nanomaterial provided great opportunity in bio-imaging and bio-detection, and could be widely promoted at relatively low cost. Further research on transferring traditional rare-earth doped systems to this new host material is also promising.

Acknowledgements

This work was financially supported by National Basic Research Program of China (973 program 2013CB733700), National Science Foundation of China (21201038 and 21231004), Shanghai Sci. Tech. Comm. (12ZR1440600 and 15QA1400700), and Fudan University's Undergraduate Research Opportunities Program (FDUROP, No. 14026). The authors also acknowledge Dr. Qianqian Su, Yuyang Gu and Xianmei Zou for discussion.

Notes and references

1 R. Y. Tsien, Annu. *Rev. Biochem.*, 1998, **67**, 509–544.
2 G. Chen, F. Tian, C. Li, Y. Zhang, Z. Weng, Y. Zhang, R. Peng and Q. Wang, *Biomaterials*, 2014, **35**, 393–400.
3 A. M. Smith, M. C. Mancini and S. Nie, *Nat. Nanotechnol.*, 2009, **4**, 710–711.
4 N. Won, S. Jeong, K. Kim, J. Kwag, J. Park, S. G. Kim and S. Kim, *Mol. Imaging*, 2012, **11**, 338–352.
5 G. Hong, J. C. Lee, A. Jha, S. Diao, K. H. Nakayama, L. Hou, T. C. Doyle, J. T. Robinson, A. L. Antaris, H. Dai, J. P. Cooke and N. F. Huang, *Circ. Cardiovasc. Imaging*, 2014, **7**, 517–525.
6 G. Hong, J. Z. Wu, J. T. Robinson, H. Wang, B. Zhang and H. Dai, *Nat. Commun.*, 2012, **3**, 700.
7 H. Yi, D. Ghosh, M.-H. Ham, J. Qi, P. W. Barone, M. S. Strano and A. M. Belcher, *Nano Lett.*, 2012, **12**, 1176–1183.
8 K. Welsher, S. P. Sherlock and H. Dai, *Proc. Natl. Acad. Sci. U. S. A.*, 2011, **108**, 8943–8948.
9 Z. Liu, X. Sun, N. Nakayama-Ratchford and H. Dai, *ACS Nano*, 2007, **1**, 50–56.
10 S. Shen and Q. Wang, *Chem. Mater.*, 2013, **25**, 1166–1178.
11 B. Dong, C. Li, G. Chen, Y. Zhang, Y. Zhang, M. Deng and Q. Wang, *Chem. Mater.*, 2013, **25**, 2503–2509.
12 Y. Zhang, G. Hong, Y. Zhang, G. Chen, F. Li, H. Dai and Q. Wang, *ACS Nano*, 2012, **6**, 3695–3702.
13 G. Hong, J. T. Robinson, Y. Zhang, S. Diao, A. L. Antaris, Q. Wang and H. Dai, *Angew. Chem., Int. Ed.*, 2012, **51**, 9818–9821.
14 S. Shen, Y. Zhang, L. Peng, Y. Du and Q. Wang, *Angew. Chem., Int. Ed.*, 2011, **50**, 7115–7118.
15 Y. Du, B. Xu, T. Fu, M. Cai, F. Li, Y. Zhang and Q. Wang, *J. Am. Chem. Soc.*, 2010, **132**, 1470–1471.
16 G. Hong, Y. Zou, A. L. Antaris, S. Diao, D. Wu, K. Cheng, X. Zhang, C. Chen, B. Liu, Y. He, J. Z. Wu, J. Yuan, B. Zhang, Z. Tao, C. Fukunaga and H. Dai, *Nat. Commun.*, 2014, **5**, 4206.
17 K. Welsher, Z. Liu, S. P. Sherlock, J. T. Robinson, Z. Chen, D. Daranciang and H. Dai, *Nat. Nanotechnol.*, 2009, **4**, 773–780.
18 S. Kruss, A. J. Hilmer, J. Zhang, N. F. Reuel, B. Mu and M. S. Strano, *Adv. Drug Deliv. Rev.*, 2013, **65**, 1933–1950.
19 S. D. Perrault, C. Walkey, T. Jennings, H. C. Fischer and W. C. W. Chan, *Nano Lett.*, 2009, **9**, 1909–1915.
20 R. Gui, H. Jin, Z. Wang and L. Tan, *Coord. Chem. Rev.*, 2015, **296**, 91–124.
21 R. Li, Z. Ji, J. Dong, C. H. Chang, X. Wang, B. Sun, M. Wang, Y. -P. Liao, J. I. Zink, A. E. Nel and T. Xia. *ACS Nano*, 2015, **9**, 3293–3306.
22 I. Villa, A. Vedda, I. X. Cantarelli, M. Pedroni, F. Piccinelli, M. Bettinelli, A. Speghini, M. Quintanilla, F. Vetrone, U. Rocha, C. Jacinto, E. Carrasco, F. S. Rodríguez, Á. Juarranz, B. del Rosal, D. H. Ortgies, P. H. Gonzalez, J. G. Solé and D. J. García, *Nano Res.*, 2015, **8**, 649–665.
23 R. Wang, X. Li, L. Zhou and F. Zhang, *Angew. Chemie Int. Ed.*, 2014, **53**, 12086–12090.
24 Z. Wang, P. Zhang, Q. Yuan, X. Xu, P. Lei, X. Liu, Y. Su, L. Dong, J. Feng and H. Zhang, *Nanoscale*, 2015, **7**, 17861–17870.
25 T. Zako, H. Hyodo, K. Tsuji, K. Tokuzen, H. Kishimoto, M. Ito, K. Kaneko, M. Maeda and K. Soga, *J. Nanomater.*, 2010, **2010**, 1–7.
26 T. Zako, M. Yoshimoto, H. Hyodo, H. Kishimoto, M. Ito, K. Kaneko, K. Soga and M. Maeda, *Biomater. Sci.*, 2015, **3**, 59–64.
27 N. Venkatachalam, T. Yamano, E. Hemmer, H. Hyodo, H. Kishimoto and K. Soga, *J. Am. Ceram. Soc.*, 2013, **96**, 2759–2765.
28 K. Soga, K. Tokuzen, K. Fukuda, H. Hyodo, E. Hemmer, N. Venkatachalm and H. Kishimoto, *J. Photopolym. Sci. Technol.*, 2012, **25**, 57–62.

Journal of Materials Chemistry B Accepted Manuscript

This journal is © The Royal Society of Chemistry 20xx

Please do not adjust margins

29 V. Mahalingam, R. Naccache, F. Vetrone and J. A. Capobianco, *Chem. - Eur. J.*, 2009, **15**, 9660–9663.
30 J. E. Geusic, H. M. Marcos and L. G. Van Uitert, *Appl. Phys. Lett.*, 1964, **4**, 182–184.
31 Y. Luo, G. Tan, G. Dong, H. Ren and A. Xia, *Ceram. Int.*, 2015, **41**, 3259–3268.
32 G. Chen, T. Y. Ohulchanskyy, S. Liu, W. Law, F. Wu, M. T. Swihart, H. Ågren and P. N. Prasad, *ACS Nano*, 2012, **6**, 2969–2977.
33 U. Rocha, K. U. Kumar, C. Jacinto, I. Villa, F. Sanz-Rodríguez, M. del Carmen Iglesias de la Cruz, A. Juarranz, E. Carrasco, F. C. J. M. van Veggel, E. Bovero, J. G. Solé and D. Jaque, *Small*, 2014, **10**, 1141–1154.
34 E. Carrasco, B. del Rosal, F. Sanz-Rodríguez, Á. J. de la Fuente, P. H. Gonzalez, U. Rocha, K. U. Kumar, C. Jacinto, J. G. Solé and D. Jaque, *Adv. Funct. Mater.*, 2015, **25**, 615–626.
35 Y. -F. Wang, G. -Y. Liu, L. -D. Sun, J. -W. Xiao, J. -C. Zhou and C. -H. Yan, *ACS Nano*, 2013, **7**, 7200–7206.
36 X. Xie, N. Gao, R. Deng, Q. Sun, Q. -H. Xu and X. Liu, *J. Am. Chem. Soc.*, 2013, **135**, 12608–12611.
37 S. Salaun, M. T. Fornoni, A. Bulou, M. Rousseau, P. Simon, and J. Y. Gesland, *J. Phys.: Condens. Matter*, 1997, **9**, 6941–6956.
38 J. Wang, F. Wang, J. Xu, Y. Wang, Y. Liu, X. Chen, H. Chen and X. Liu, *C. R. Chim.*, 2010, **13**, 731–736.
39 F. Wang, R. Deng and X. Liu, *Nat. Protoc.*, 2014, **9**, 1634–1644.
40 A. Dong, X. Ye, J. Chen, Y. Kang, T. Gordon, J. M. Kikkawa and C. B. Murray, *J. Am. Chem. Soc.*, 2011, **133**, 998–1006.
41 L. Xiong, Z. Chen, Q. Tian, T. Cao, C. Xu and F. Li, *Anal. Chem.*, 2009, **81**, 8687–8694.
42 S. A. Miller, H.E. Rast and H.H. Caspers. *J. Chem. Phys.*, 1970, **52**, 4172–4175.
43 V. Mahalingam, F. Vetrone, R. Naccache, A. Speghini and J. A. Capobianco, *Adv. Mater.*, 2009, **21**, 4025–4028.
44 J. Peng, Y. Sun, L. Zhao, Y. Wu, W. Feng, Y. Gao and F. Li. *Biomaterials*, 2013, **34**, 9545–9544.
45 K. Brindle, *Nat. Rev. Cancer*, 2008, **8**, 94–107.
46 G. Hong, J. C. Lee, J. T. Robinson, U. Raaz, L. Xie, N. F. Huang, J. P. Cooke and H. Dai, *Nat. Med.*, 2012, **18**, 1841–1846.
47 P. V. AshaRani, G. Low Kah Mun, M. P. Hande and S. Valiyaveettil, *ACS Nano*, 2009, **3**, 279–290.
48 C.-W. Lam, J. T. James, R. McCluskey, S. Arepalli and R. L. Hunter, *Crit. Rev. Toxicol.*, 2006, **36**, 189–217.
49 J. Peng, Y. Sun, Q. Liu, Y. Yang, J. Zhou, W. Feng, X. Zhang and F. Li, *Nano Res.*, 2012, **5**, 770–782.

Journal of Materials Chemistry B Accepted Manuscript

Please do not adjust margins

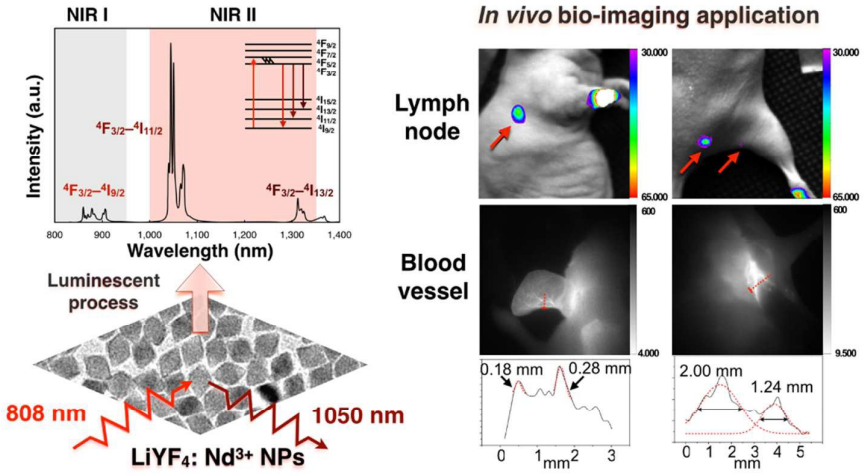

In vivo bioimaging of high spatial resolution based on $LiYF_4$: Nd in the second near-infrared window.

Journal of Materials Chemistry B Accepted Manuscript